Research Square

Preprints are preliminary reports that have not undergone peer review.
They should not be considered conclusive, used to inform clinical practice,
or referenced by the media as validated information.

Targeting LSD1 inhibits gastric cancer by reprogramming macrophages and restoring T-cell response

Yi-Chao Zheng

yichaozheng@zzu.edu.cn

Zhengzhou University https://orcid.org/0000-0002-2662-3770

Jingru Pang

Zhengzhou University

Yu Zhang

Zhengzhou University

Haoyi Zhu

Zhengzhou University

Dan-Dan Shen

Zhengzhou University

Bo Wang

Zhengzhou university

Yan Li

The University of Auckland

Guo-Liang Lu

The University of Auckland

Ning Wang

The University of Hong Kong https://orcid.org/0000-0003-1410-329X

Zheng-Hong Yang

ZhengZhou University

Xingjie Dai

Hong-Min Liu

Zhengzhou University

Article

Keywords: Gastric cancer, LSD1, Quinoline-based LSD1 inhibitor, Macrophage polarization, CD8+ T-cell exhaustion

Posted Date: July 1st, 2026

DOI: https://doi.org/10.21203/rs.3.rs-10063093/v1

License: This work is licensed under a Creative Commons Attribution 4.0 International License.
Read Full License

Additional Declarations: (Not answered)

Targeting LSD1 inhibits gastric cancer by reprogramming macrophages and restoring T-cell response

Jing-Ru Pang[1, 2], Yu Zhang[1, 2], Hao-Yi Zhu[1, 2], Dan-Dan Shen[4], Bo Wang[1, 2], Yan Li[5, 6], Guo-Liang Lu[6, 7], Ning Wang[8], Zhenghong Yang[2, 9], Hong-Min Liu[1, 2, *], Xing-Jie Dai[1, 2, *] Yi-Chao Zheng[1, 2, 3, *]

[1] Key Laboratory of Advanced Drug Preparation Technologies, Ministry of Education of China; Key Laboratory of Henan Province for Drug Quality and Evaluation; XNA platform, School of Pharmaceutical Sciences, Zhengzhou University, Zhengzhou, Henan 450001, China.

[2] State Key Laboratory of Metabolic Dysregulation & Prevention and Treatment of Esophageal Cancer, Zhengzhou, Henan 450001, China.

[3] Pingyuan Laboratory, Xinxiang, Henan 450001, China.

[4] Department of Obstetrics and Gynecology, The Third Affiliated Hospital of Zhengzhou University,450052, Henan, China.

[5] Department of Biomedicine and Medical Diagnostics, School of Science, Auckland University of Technology. 34 St. Paul Street, Auckland 1010, New Zealand.

[6] Maurice Wilkins Centre, The University of Auckland, Private Bag 92019, Auckland 1142, New Zealand.

[7] Auckland Cancer Society Research Centre, Faculty of Medical and Health Sciences, The University of Auckland, Private Bag 92019, Auckland 1142, New Zealand.

[8] School of Chinese Medicine, the University of Hong Kong, 3, Sasson Road, Pokfulam, Hong Kong.

[9] Tianjian Laboratory of Advanced Biomedical Sciences, Academy of Medical Sciences, Zhengzhou University, Zhengzhou 450052, China.

*Corresponding authors: Hong-Min Liu (liuhm@zzu.edu.cn), Xing-jie Dai (dxj@zzu.edu.cn), Yi-Chao Zheng (yichao.zheng@hotmail.com).

Abstract

The heightened expression of lysine-specific demethylase 1 (LSD1/KDM1A) in multiple malignancies facilitates immune evasion, aiding in tumor survival; however, its role in shaping the gastric cancer (GC) tumor immune microenvironment remains incompletely defined. Here, we show that loss of tumor cell-intrinsic LSD1 skews M0 macrophage polarization into an anti-tumor M1 phenotype, enhances $CD8^+$ T-cell recruitment and activation, and attenuates $CD8^+$ T-cell exhaustion by suppressing M0 macrophage polarization into the pro-tumor M2 phenotype. Guided by these insights, we designed a quinoline-based reversible inhibitor series. Lead compound KL-1 suppresses LSD1 (IC_{50} = 18 nM) and reprograms macrophage–T-cell crosstalk in vivo. In a syngeneic GC model, KL-1 elicits robust tumor growth inhibition accompanied by increased intratumoral M1 macrophages and functional $CD8^+$ T cells; depletion of either macrophages or $CD8^+$ T cells abrogate the efficacy, establishing their necessity for response. These findings position LSD1 as a tractable epigenetic node for immune reprogramming in GC and identify KL-1 as a promising clinical candidate.

Key words

Gastric cancer; LSD1; Quinoline-based LSD1 inhibitor; Macrophage polarization; $CD8^+$ T-cell exhaustion.

Introduction

Globally, GC ranks fifth among malignancies contributing to cancer mortality, with a five-year survival rate under 10% for advanced-stage disease[1-5]. Although clinical outcomes have improved in multimodal treatments like surgery, chemotherapy, immunotherapy, and targeted therapy, the benefits remain limited due to late diagnosis, frequent drug resistance, and low response rates to immune checkpoint inhibitors[2, 3, 6, 7]. These difficulties stress the pressing necessity for new therapeutic strategies capable of overcoming immune evasion and improving long-term survival.

LSD1, also called KDM1A, is overexpressed in various malignancies and is implicated in tumorigenesis and progression[8-10]. In malignancies such as prostate cancer, esophageal cancer, and GC, LSD1 drives tumor proliferation, invasion, and metastasis[11-13]. Importantly, emerging evidence suggests that LSD1 is a significant factor in modulating the tumor immune microenvironment[14]. LSD1 inhibitors can boost the cytotoxic function of natural killer cells[15-19]. LSD1 is also involved in germinal-center B cell maturation[20], and its inhibition enhances the potency of PD-1/PD-L1 checkpoint blockade in melanoma and breast cancer by augmenting T-cell infiltration[10, 21, 22]. Besides, LSD1 contributes to the immunosuppressive functions of tumor-associated fibroblasts (CAFs)[21, 23]. Although the broader role of LSD1 in cancer immune modulation is established, its specific impact on the immune microenvironment in GC is not well understood.

Current LSD1 inhibitors are categorized structurally into phenylcyclopropylamine-based, peptide-like, and polyamine analogues[24-26].

Among these, phenylcyclopropylamine-based LSD1 inhibitors are the most advanced in clinical trials[27]; however, they often exhibit poor selectivity against LSD1 and carry potential toxicity risks[24, 28]. Reversible LSD1 inhibitors, while offering potential advantages in safety and phenotypic outcomes[29, 30], still face challenges in potency and selectivity, with only a few compounds–CC-90011, X-L177, and SP-2577–progressing into clinical evaluation so far[31]. Thus, there is a pressing need for novel drug design strategies to develop innovative LSD1-targeting agents to inject new momentum into this field and guide future research directions.

Our previous work demonstrated that LSD1 deletion inhibited tumor growth in immunocompetent but not immunodeficient mice[8], suggesting an immune-dependent mechanism. To further explore this, single-cell RNA sequencing (scRNA-seq) was conducted on $CD45^+$ immune cells sorted from the subcutaneous tumors in mice. The analysis revealed that T cells and macrophages were the predominant immune populations in the GC microenvironment and were significantly affected by LSD1 ablation. Specifically, LSD1 deletion enhanced the abundance of anti-tumor M1 macrophages and activated $CD8^+$ T cells, while reducing pro-tumor M2 macrophages and exhausted $CD8^+$ T cells ($CD8^+$ T_{ex}). These observations led us to hypothesize and validate that LSD1 promotes immune evasion by reshaping macrophage phenotypes and impairing $CD8^+$ T-cell function.

To develop novel LSD1 inhibitors, we redesigned the quinazoline-based inhibitor Z-1[32] through bioisosteric replacement by substituting a nitrogen atom in the quinazoline ring with a carbon atom, yielding the quinoline derivative compound 1,

which was subsequently subjected to further structural optimization. These efforts culminated in compound 29 (KL-1), a highly potent LSD1 inhibitor (IC_{50} = 0.018 μM). We further confirmed that inhibition of LSD1 with our potent inhibitor KL-1 reproduced these effects – suppressing tumor growth through reprogramming of macrophage polarization and restoration of $CD8^+$ T-cell anti-tumor functionality. Collectively, these results identify LSD1 as a significant mediator of tumor immune suppression and highlight its promise as a therapeutic target to reshape the immune microenvironment, thereby providing a promising clinical candidate.

Results

LSD1 suppresses the tumor immune microenvironment via macrophages and T cells in GC

To explore the effect of LSD1 in the tumor immune microenvironment, we generated LSD1 knockout mouse forestomach carcinoma (MFC) cells using CRISPR-Cas9 (Fig. S1A), implanted them into immunocompetent mice, isolated $CD45^+$ tumor-infiltrating lymphocytes (TILs) from subcutaneous tumors, and conducted scRNA-seq. A total of 30,415 $CD45^+$ cells were profiled, revealing 27 distinct immune clusters (Fig. 1A). Marker gene analysis revealed that macrophages, monocytes, T cells, NK cells, and B cells were the primary immune populations, with macrophages being the most prevalent subset (Fig. 1B-D). Comparative analysis revealed a modest reduction in macrophage proportion and a notable elevation in T cells in the LSD1 knockout (KO) group relative to the control (CON) group (Fig. 1D). Further clustering of 16,011 macrophages revealed 11 subtypes that were annotated as M1 or M2 macrophages

based on representative marker genes (Fig. 1E and Fig. S1B-D). LSD1 KO tumors exhibited a notable rise in M1 macrophages along with a reduction in M2 macrophages (Fig. 1D). Similarly, analysis of 3,467 T cells identified eight clusters, including $CD8^+$ T_{ex}, $CD4^+$ T_{mem}, and regulatory T-cell subsets (Fig. 1F and Fig. S1E-G). Notably, the abundance of $CD8^+$ T_{ex} was significantly reduced in the LSD1 knockout group (Fig. 1G). Collectively, these findings imply that LSD1 might be involved in regulating macrophage and T-cell subtypes, potentially suppressing the tumor immune microenvironment.

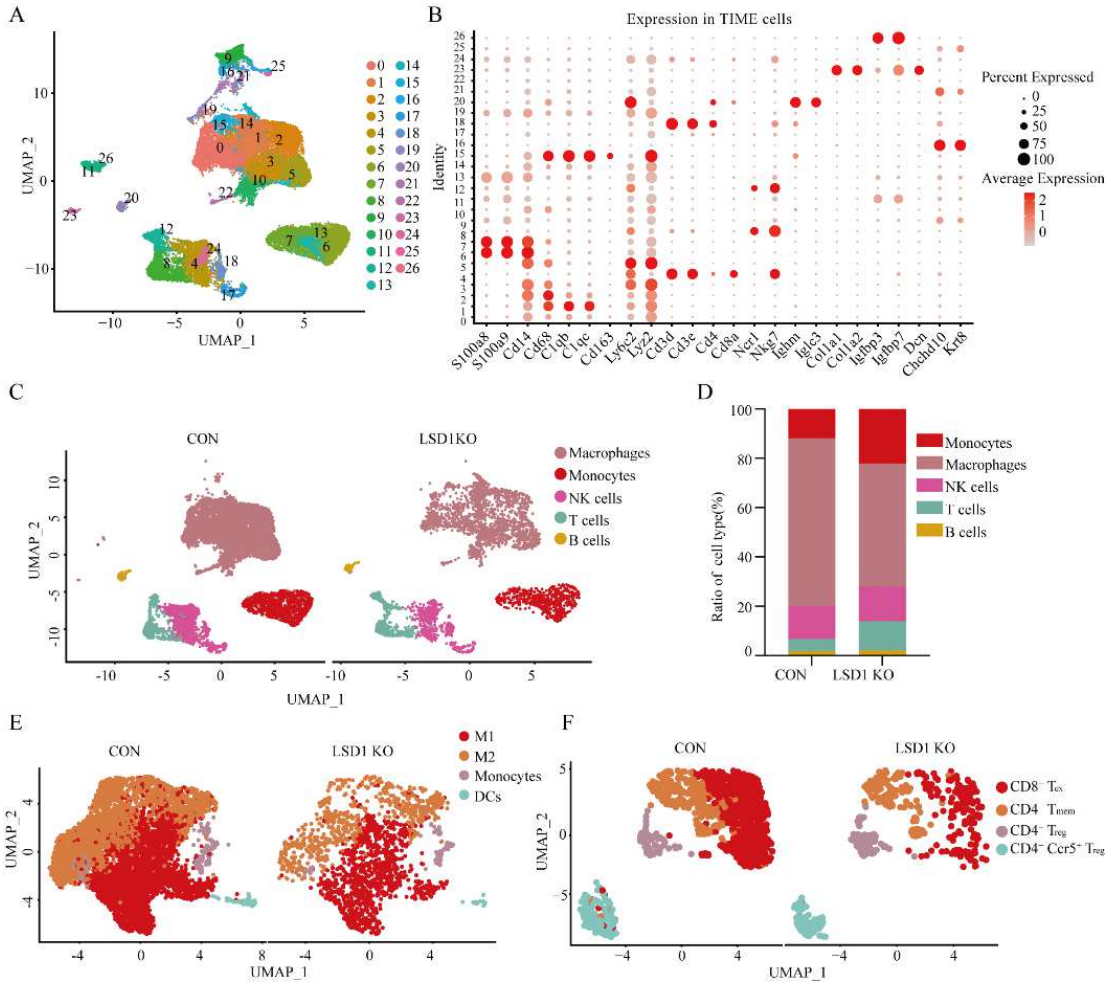


Fig. 1 LSD1 suppresses the tumor immune microenvironment via macrophages and T cells in GC. A UMAP plot showcasing single-cell transcriptomes from TILs, colored by cluster identity. B

Dot plot showing expression of specific marker genes identified clusters in TILs. C UMAP visualization of immune cell aggregations from MFC CON and MFC LSD1 KO tumors. Dots represent individual cells, and colors indicate distinct clusters. D Proportions of immune cell subsets in MFC CON and MFC LSD1 KO groups. E UMAP plots of macrophage-related clusters in MFC CON and MFC LSD1 KO groups. M1, M1 macrophages; M2, M2 macrophages; DCs, dendritic cells. F UMAP plots showing integrated T-cell clusters in MFC CON and MFC LSD1 KO groups. $CD8^+$ T_{ex} refers to exhausted $CD8^+$ T cells; $CD4^+$ T_{mem} denotes $CD4^+$ memory T cells; $CD4^+$ Treg indicates $CD4^+$ regulatory T cells; $CD4^+Ccr5^+$ Treg specifies $CD4^+Ccr5^+$ regulatory T cells.

LSD1 promotes tumor progression by facilitating M2 macrophage polarization while inhibiting M1 macrophage polarization.

To investigate the regulatory effects of tumor cell-intrinsic LSD1 on macrophages, clodronate liposomes or PLX3397 were used to clear macrophages in immunocompetent mice prior to subcutaneous implantation of MFC CON or MFC LSD1 KO cells (Fig. 2A; Fig. S2A). In the LSD1 KO group, tumor suppression was partially diminished in the macrophage-depleted mice relative to immunocompetent mice, indicating that macrophages were involved in the anti-tumor effect of LSD1 deficiency (Fig. 2B-D; Fig. S2B-D). However, LSD1 deletion continued to inhibit tumor proliferation compared to controls under macrophage depletion, suggesting that additional immune cells were involved in LSD1 deletion-mediated anti-tumor activity (Fig. 2B-D; Fig. S2B-D). Building on the scRNA-seq data indicating that LSD1 may modulate the proportions of M1 and M2 macrophages (Fig. S1D), we further investigated its regulatory role on macrophage polarization. Flow cytometry revealed

no notable variation in total macrophage abundance between MFC CON and MFC LSD1 KO groups (Fig. S2E), but the MFC LSD1 KO group showed increased M1 and decreased M2 macrophage populations (Fig. 2E, F), consistent with immunofluorescence results (Fig. S2F, G). To validate these findings *in vitro*, LSD1 knockout and control AGS and MKN45 cells were generated (Fig. S2H), and conditioned media (CM) from these cells were used to treat PMA-induced THP-1 macrophages (M0). CM from the LSD1 knockout GC cells drived M0 macrophages toward the anti-tumor M1 macrophages (CD86, CD80) while suppressing their differentiation into the pro-tumor M2 macrophages (CD206, CD163) (Fig. 2G and H; Fig. S2I, J). Similar effects were observed in RAW264.7 macrophages exposed to CM from MFC CON or MFC LSD1 KO cells (Fig. S2K). To assess the effects of LSD1 on macrophage recruitment, chemotactic migration assays were conducted and the results showed that LSD1 knockout tumor cells enhanced M1 macrophage migration, while suppressing M2 migration compared to controls (Fig. 2I, J; Fig. S2L). Together, these findings suggest that tumor cell-intrinsic LSD1 promotes tumor growth by reprogramming M0 macrophages, driving their skewing into the pro-cancer M2 phenotype and enhancing M2 recruitment, while simultaneously blocking their differentiation toward the anti-tumor M1 phenotype and limiting M1 recruitment.

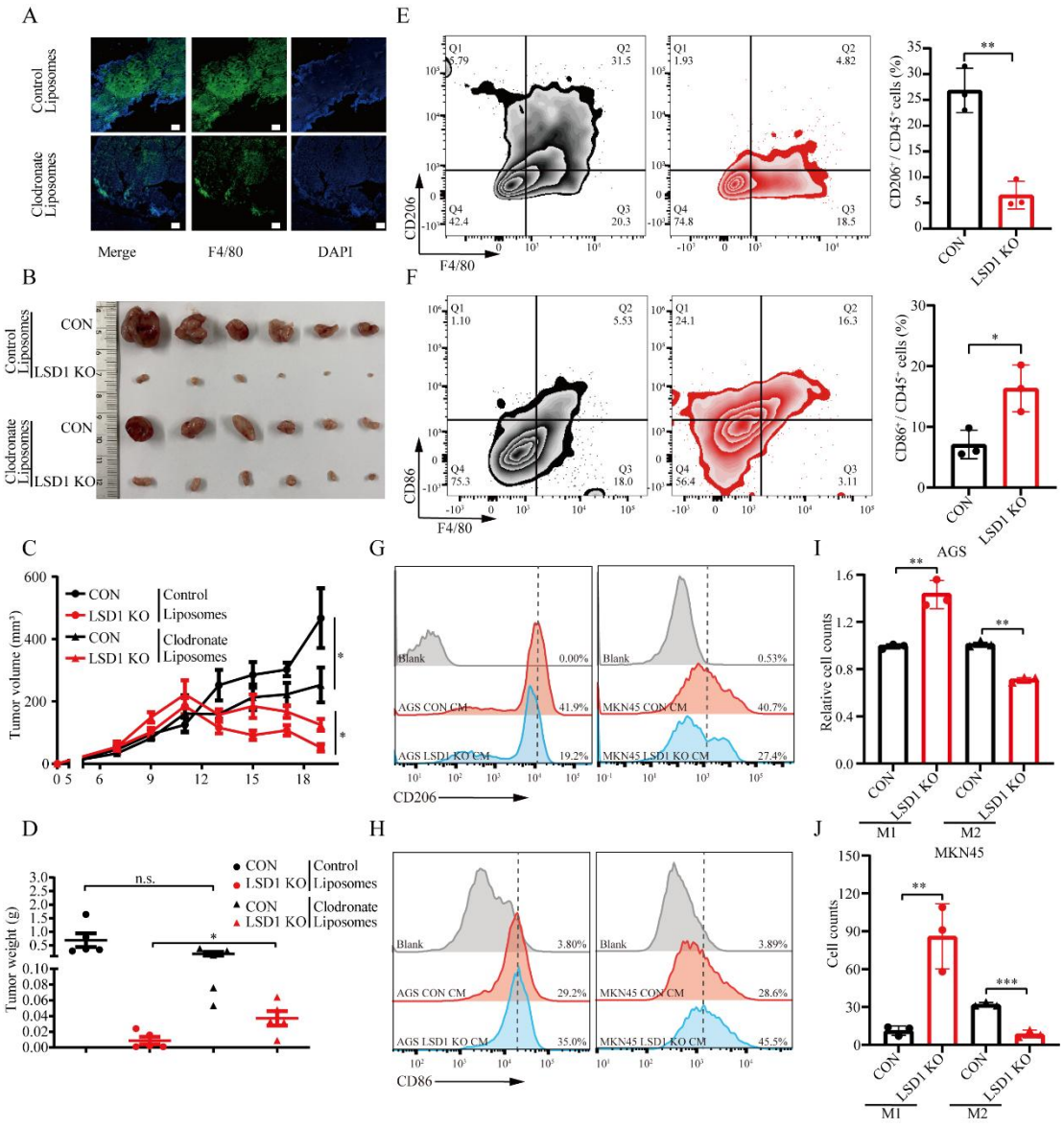


Fig. 2 LSD1 promotes tumor progression by facilitating M2 macrophage polarization while inhibiting M1 macrophage polarization. A Representative images showing macrophage depletion in the spleen of 615 mice. Scale bar, 50 μm. B-D Following macrophage depletion, MFC cells with or without LSD1 knockout were inoculated subcutaneously into 615 mice. Images of tumors (B), along with measurements of tumor volume (C) and weight (D). Data are shown as mean ± SD; $n = 6$. E and F Proportions of $F4/80^{+}CD206^{+}$ (E) and $F4/80^{+}CD86^{+}$ (F) macrophages in TILs from control and LSD1 knockout tumors, as determined by flow cytometry. G and H Proportions of M0 macrophages polarized to $CD206^{+}$ (G) and $CD86^{+}$ (H) phenotypes following exposure to CM from

LSD1 knockout or control AGS and MKN45 cells. I and J Chemotactic migration of M1 and M2 macrophages co-incubated with AGS (I) and MKN45 cells (J) Data are represented as mean ± SD; $n = 3$; two-tailed unpaired Student's *t*-test; n.s., no significance, $*p < 0.05$, $**p < 0.01$, $***p < 0.001$.

LSD1 drives GC progression by suppressing $CD8^+$ T-cell activity and promoting M2 macrophage-mediated $CD8^+$ T-cell exhaustion.

ScRNA-seq analysis showed a markedly higher proportion of T cells in the MFC LSD1 KO group compared to the MFC CON group (Fig. 1D). Consistent with this, our previous study demonstrated that tumor cell-intrinsic LSD1 deletion inhibits tumor growth in immunocompetent but not immunodeficient mice[8], suggesting a role for LSD1 in suppressing T cell-driven anti-tumor immunity. Additionally, flow cytometric analysis revealed a notable rise in $CD8^+$ T cells in the LSD1 knockout group (Fig. 3A and Fig. S3A). Moreover, CM from the LSD1 knockout GC cells enhanced $CD8^+$ T-cell activation relative to the control groups, as indicated by elevated CD69 and CD25 expression (Fig. 3B, C; Fig. S3B, C), indicating that LSD1 dampens $CD8^+$ T-cell activation. ScRNA-seq analysis also demonstrated a strong reduction of $CD8^+$ T_{ex} in the LSD1 KO tumors (Fig. S1G). However, direct co-culture of T cells with CM from LSD1 knockout or control GC cells did not alter the expression of LAG-3, Tim-3, and PD-1 (Fig. S3D, F), suggesting that LSD1 may regulate T-cell exhaustion indirectly. Given the well-established interplay between macrophages and T cells within the immune system, and our aforementioned findings demonstrating that LSD1 regulates macrophage polarization, we hypothesize that macrophages may mediate the effectiveness of LSD1 on T cell function. Flow cytometry confirmed that macrophage

depletion eliminated the increase in $CD8^+$ T cells induced by LSD1 knockout in tumor cells (Fig. 3D; Fig. S3G), supporting the notion that macrophages may serve as key intermediaries in LSD1-driven modulation of $CD8^+$ T-cell enrichment. *In vivo* immune cell depletion studies further demonstrated that tumor cell-intrinsic LSD1 deficiency suppressed tumor growth most effectively in immunocompetent mice, with progressively diminishing effects following the depletion of macrophages, T cells, and both populations (Fig. 3E, F), underscoring a predominant role for $CD8^+$ T cells. Further flow cytometry experiments showed that LSD1 deletion promoted the M1 phenotype and $CD8^+$ T-cell enrichment while suppressing the M2 macrophages (Fig. 3G, H; Fig. S3H-J). Notably, macrophage depletion abrogated the $CD8^+$ T-cell enrichment induced by LSD1 deficiency, while $CD8^+$ T-cell depletion eliminated the differences in M1 and M2 phenotypes within tumor immune microenvironment observed upon LSD1 loss (Fig. 3G and H; Fig. S3H-J), suggesting that tumor cell-intrinsic LSD1 may orchestrate macrophage-T cell crosstalk. Given prior reports of M2-driven $CD8^+$ T-cell exhaustion[33, 34], we hypothesized that LSD1 may indirectly promote $CD8^+$ T-cell exhaustion by facilitating the M2 macrophage phenotype. Indeed, M2 macrophages induced from THP-1 cells recapitulated LSD1-mediated $CD8^+$ T-cell exhaustion in co-culture assays (Fig. 3I-L). Based on the aforementioned findings that LSD1 promotes M0 macrophage polarization into the M2 phenotype, this study identified that LSD1 facilitates $CD8^+$ T-cell exhaustion by this mechanism. Collectively, these findings reveal that tumor cell-intrinsic LSD1 fosters an immunosuppressive microenvironment to support gastric cancer progression by inhibiting $CD8^+$ T-cell activation, along with

promoting CD8⁺ T-cell exhaustion by driving the shift of M0 macrophages to the M2 phenotype.

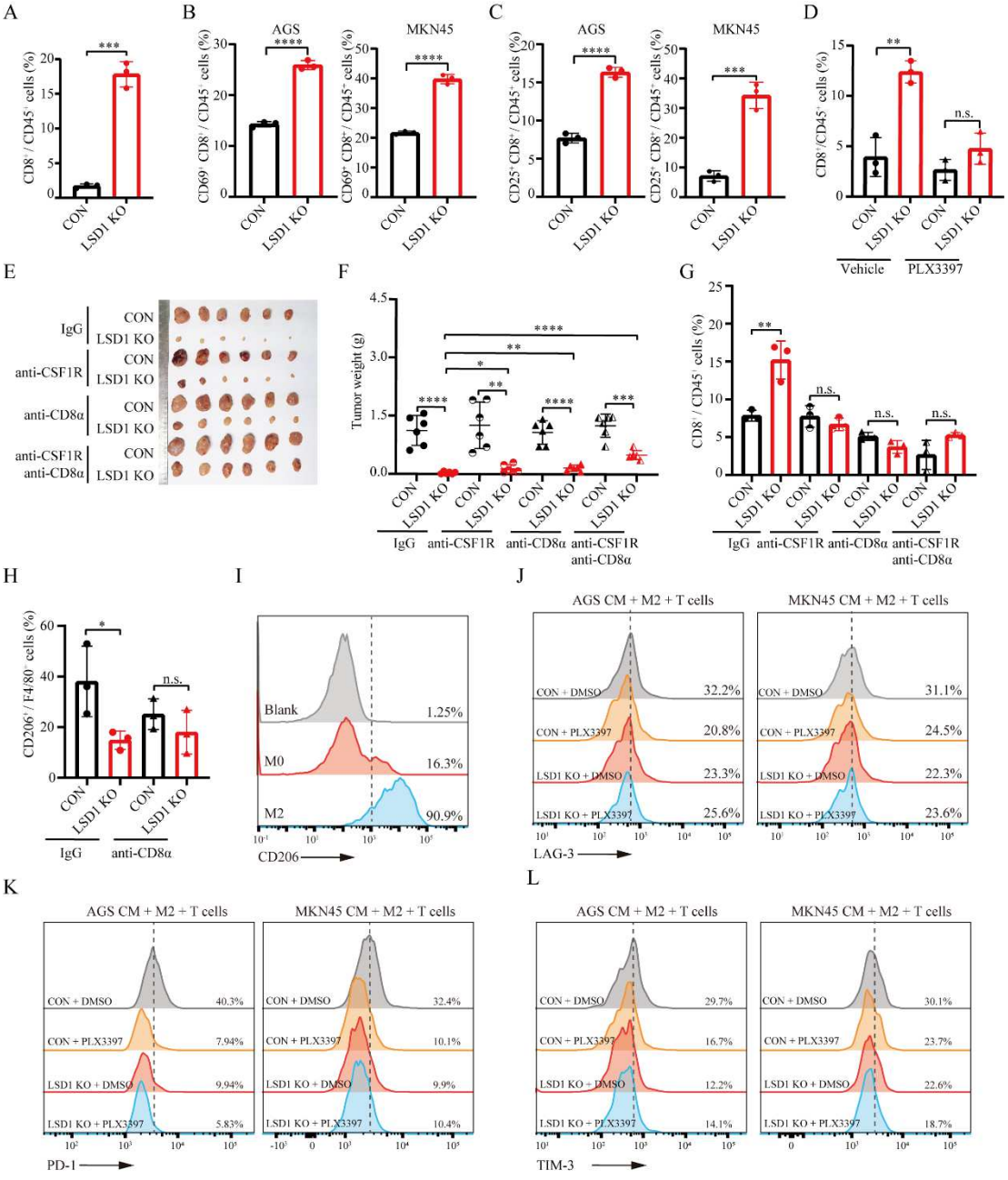


Fig. 3 LSD1 drives GC progression by hindering CD8⁺ T-cell activity and promoting M2 macrophage-induced CD8⁺ T-cell exhaustion. A Flow cytometry determined the frequency of CD8⁺ T cells in TILs from both MFC control and MFC LSD1 knockout tumors. B and C Flow cytometric analysis of the frequency of CD8⁺CD69⁺ T cells (B) and CD8⁺CD25⁺ T cells (C) after co-culture with CM from LSD1 knockout or control AGS and MKN45 cells. D Proportions of CD8⁺ T cells in

TILs from 615 mice bearing MFC CON or MFC LSD1 KO tumors following macrophage depletion, as determined by flow cytometry. E and F Tumor images at the experimental endpoint (E) and tumor weights (F) of 615 mice bearing MFC control or MFC LSD1 knockout cells following macrophage or $CD8^+$ T-cell depletion. Data are presented as mean ± SD, $n = 6$. G and H $CD45^+CD8^+$ cells (G) and $F4/80^+CD206^+$ macrophages (H) in TILs of tumors from 615 mice. I Proportions of THP-1 induced into M2 macrophages. J-L Expression of LAG-3 (J), PD-1 (K), and TIM-3 (L) following 8-day co-incubation of T cells with M2 macrophages pretreated with CM from LSD1 knockout or control AGS and MKN45 cells. Data are presented as the mean ± SD; $n = 3$; two-tailed unpaired Student's *t*-test; n.s., no significance; $^{****}p < 0.0001$, $^{***}p < 0.001$, $^{**}p < 0.01$, $^{*}p < 0.05$.

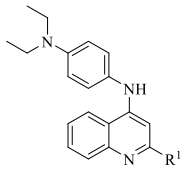
Development and biological assessment of KL-1 as an LSD1 inhibitor

To improve the inhibitory potency of quinazoline-based LSD1 inhibitors and develop novel reversible chemotypes, we selected compound Z-1[32] as a lead structure. Key pharmacophores essential for LSD1 binding–the *o*-phenylenediamine and methanesulfonylphenyl motifs–were retained. A bioisosteric replacement strategy was applied to the quinazoline core, replacing the N atom with carbon to afford the quinoline derivative 1 (Fig. 4A). Molecular docking indicated that 1 adopts a Y-shaped conformation within the LSD1 active site: the aminophenylenediamine group occupies the hydrophobic subpocket, while the methanesulfonylphenyl moiety binds in the hydrophilic region, forming a hydrogen bond with Val288. Additionally, the quinoline core engages the neutral cavity via H–π and π–π interactions with Tyr761, Trp751, and Gly330 (Fig. 4A). Although 1 showed moderate LSD1 inhibition (IC_{50} = 0.760 μM) relative to Z-1, its binding mode supported further optimization. Subsequent structure-

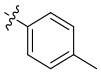
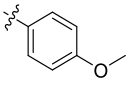
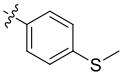
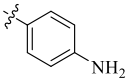
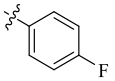
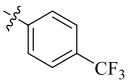
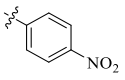
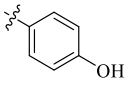
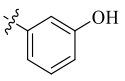
based design integrated FAD mimicry and molecular hybridization approaches to modify the R^1, R^2, and R^3 positions of the quinoline scaffold.

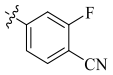
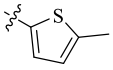
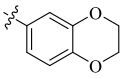
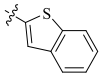
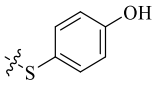
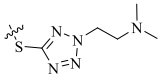
Firstly, we systematically modified the R1 methanesulfonyl-phenyl group, introducing various substituents, heterocycles, and known LSD1-active fragments–such as thiol-tetrazole and 3-fluoro-4-cyanophenyl–resulting in compounds 2 to 24 (Table 1)[35]. Structure-activity relationship (SAR) suggested that electron-donating groups on the phenyl ring improved potency in the order: OH > SCH_3 > OCH_3 > NH_2 > CH_3, with compound 10 (p-OH) exhibiting a ~10-fold increase in potency over 1 (Fig. 4B). Shifting the OH group to ortho- or meta-positions led to sharp activity decline. While para-substituted electron-withdrawing groups generally reduced activity, para-fluoro substitution (14) offered a modest ~10-fold gain, albeit still inferior to compound 10. Replacing the phenol moiety with methyl or hydrogen reduced activity by ~6-fold, and introducing sulfur linkers further diminished potency. Among heterocyclic modifications, five-membered rings–particularly the furan group in 18–outperformed others, offering an ~11-fold improvement over 1 (Fig. 4B). Only benzothiophene among the fused rings retained inhibitory activity. Conversely, incorporation of known LSD1-active fragments such as 3-fluoro-4-cyanophenyl (compound 13)[36] or mercaptotetrazole (compound 24)[35] via molecular hybridization led to a significant decrease in LSD1 inhibition (Fig. 4B). Collectively, these results identified the furan ring as the optimal R1 substituent for enhancing LSD1 binding affinity and inhibitory potency.

267 Table 1. Chemical structures and corresponding biochemical activities of compounds 2–24.



268

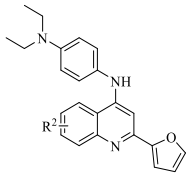
Compound	R1	Inhibition at 10 μM	IC50（μM）
2		90.45%	0.148±0.002
3		85.85%	0.611±0.002
4		93.39%	0.170±0.002
5		94.19%	0.142±0.002
6		90.23%	0.426±0.003
7		97.85%	0.081±0.002
8		84.63%	0.625±0.002
9		71.88%	3.217±0.195
10		99.63%	0.075±0.002
11		83.61%	1.058±0.024
12		90.17%	0.819±0.003

13		87.29%	1.835±0.064
14	H	80.69%	0.433±0.003
15	Me	82.94%	0.453±0.003
16		85.39%	0.673±0.003
17		79.63%	1.990±0.019
18		99.89%	0.070±0.002
19		93.58%	0.167±0.002
20		89.85%	0.138±0.003
21		21.39%	＞10
22		97.69%	0.241±0.002
23		71.95%	5.915±0.772
24		20.99%	＞10
CC-90011	-	100%	0.003

Molecular docking simulations of compound 1 bound to LSD1 revealed that the quinoline ring occupied the neutral region of the LSD1 active site. Structural analysis indicated that modifications at positions 6 and 7 on the phenyl ring would not disrupt

the Y-shaped binding conformation. Consequently, to enhance binding affinity and inhibitory activity, various substituents were introduced at the 6- and 7-positions of the phenyl ring, generating compounds 25–31 (Table 2). Among them, compound 29, with a 6-fluoro group, demonstrated significantly improved LSD1 inhibitory activity (IC_{50} = 0.018 μM) compared to compounds 18 and the original Z-1, highlighting 6-fluoro substitution as optimal for R2-site modification (Fig. 4B and Table 2).

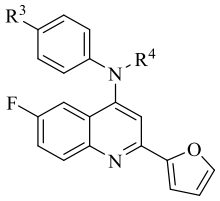
Table 2. Chemical structures and corresponding biochemical activities of compounds 25–31.



Compound	R2	Inhibition at 10 μM	IC50（μM）
25	6-Me	96.38%	0.135 ± 0.002
26	7-Me	89.75%	0.399±0.003
27	7-OMe	90.12%	1.052±0.075
28	7-Cl	32.19%	＞10
29 (KL-1)	6-F	99.57%	0.018±0.002
30	6-CF3	92.96%	0.096±0.003
31	6-NO2	81.29%	0.704±0.002
CC-90011	-	100%	0.003

Based on the strong LSD1 inhibitory effect observed with compound 29, structural optimization was further explored at the R3 and R4 positions. First, the role of the diethylamino group was assessed by modifying this moiety to generate compounds 32–35 (Table 3). Elimination or replacement of the diethylamino group resulted in a marked reduction in LSD1 inhibition, confirming that the aminodiphenylamine motif is essential for maintaining activity (Fig. 4B and Table 3). To evaluate whether the free amino group at the R4 position is similarly critical, a methyl group was introduced at this site in compound 29, generating compound 36. *In vitro* enzymatic assays revealed a significant decrease in LSD1 inhibitory potency for compound 36 relative to 29, demonstrating the importance of a free amino group for optimal LSD1 interaction (Fig. 4B). These findings collectively indicate that both the diethylamino moiety and the free amine at the R4 position are key structural features required for optimal LSD1 inhibition.

Table 3. Chemical structures and corresponding biochemical activities of compounds 32–36



Compound	R3	R4	Inhibition at 10 μM	IC50（μM）
32	H	H	17%	＞10
33	Me	H	19%	＞10
34	OMe	H	26%	＞10
35	Morpholine	H	29%	＞10
36	Diethylamino	Me	9.17%	＞10
CC-90011	-	-	100%	0.003

Taken together, among all 36 synthesized compounds, compound 29 demonstrated the strongest LSD1 inhibition. Molecular docking simulations uncovered that compound 29 occupies the cavity in a Y-shaped conformation, showing good overlap with the hydrophilic side chain portion of FAD (Fig. 4C). The aminophenylenediamine moiety extends into the hydrophobic region of the LSD1 active site, where its amino group establishes a stable hydrogen bond with the amino acid residue Glu801. The diethylaminophenyl group occupied the cavity and contributes to the conformation. The furan moiety extends into the hydrophilic region of the LSD1 active site, where the furan ring forms a defined H–π interaction with the amino acid residue Gly287. The

quinoline scaffold occupies the neutral region of the LSD1 active site and stabilizes the conformation, with the N atom at position 1 of the pyrimidine ring engaging in a key hydrogen bond contact with the amino acid residue Ser289. Since Gly287, Ser289, and Glu801 all form strong hydrogen bond interactions with FAD, it can be inferred that compound 29 acts in an FAD-competitive binding mode, occupying the LSD1 active site and thereby affecting the biological function of LSD1 to exert an inhibitory effect on its activity.

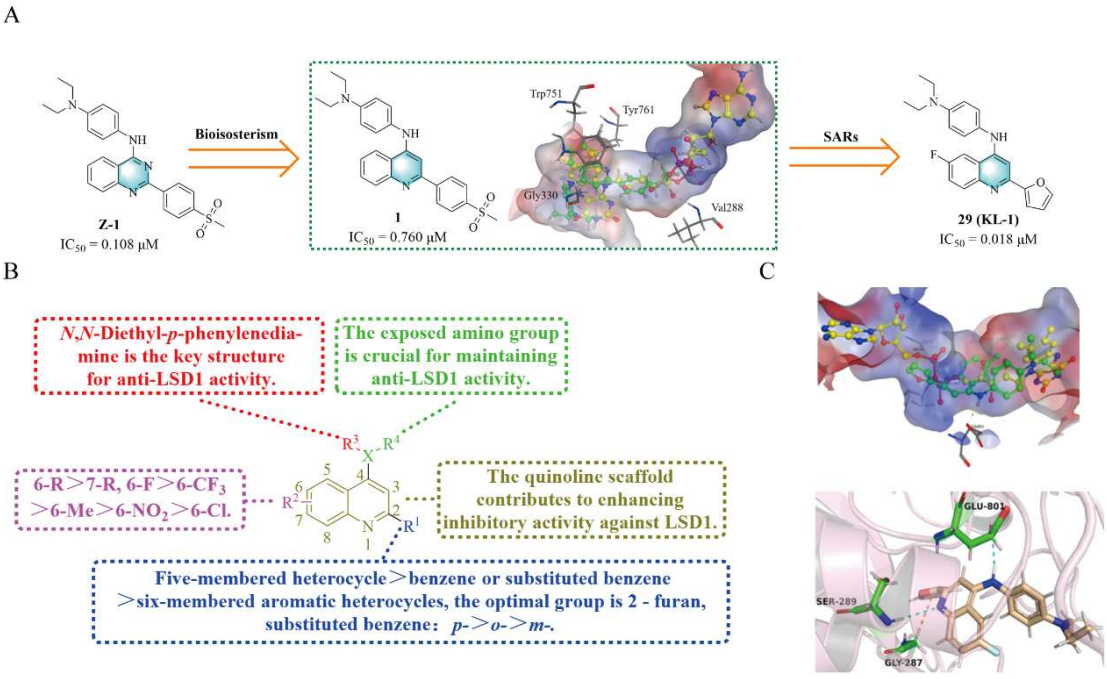
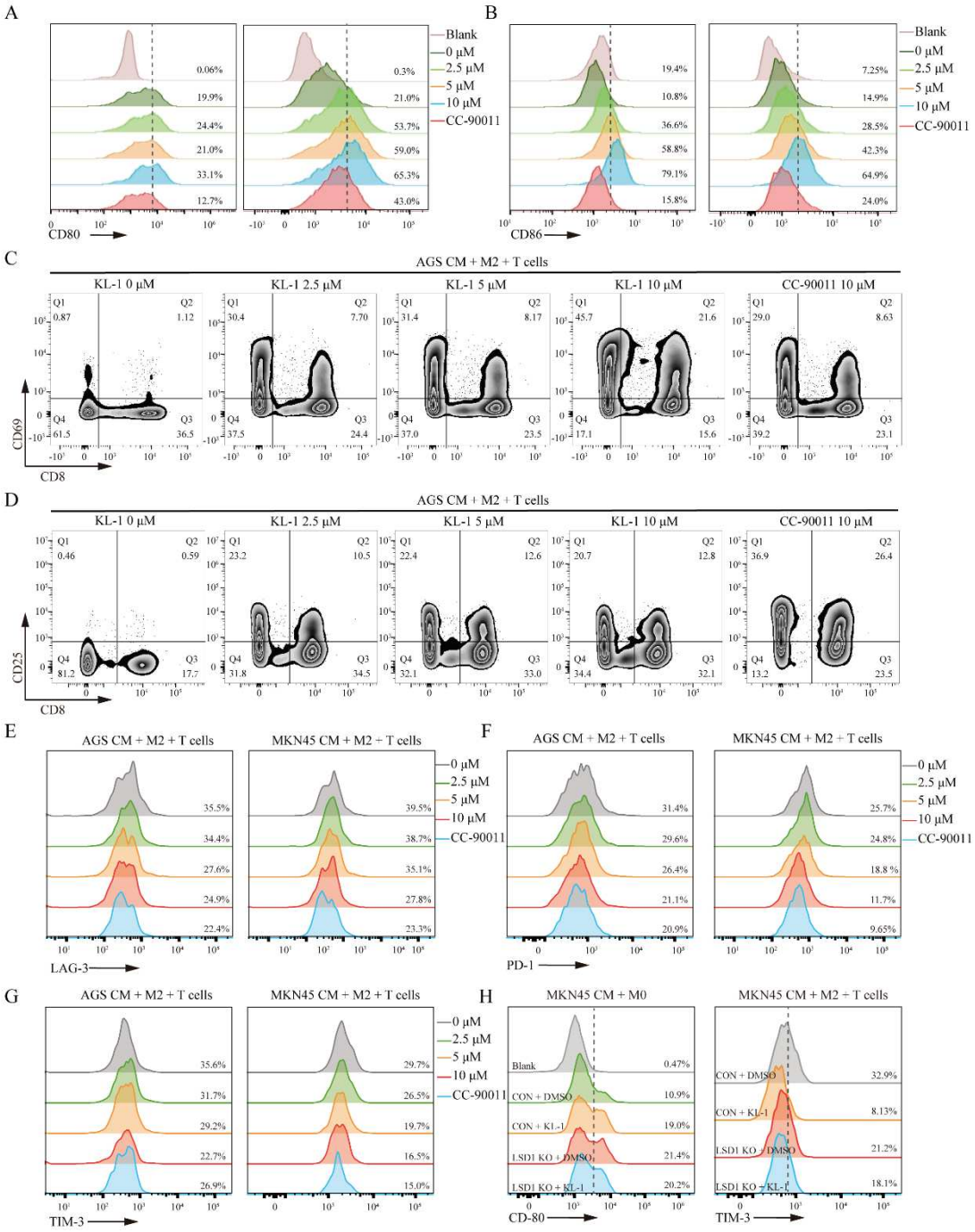


Fig. 4 Development and biological evaluation of KL-1 as an LSD1 inhibitor. A Design strategy of quinoline-based LSD1 Inhibitors. B Summary of the SAR of quinoline-derived LSD1 inhibitors. C Molecular docking model of compound 29 bound to LSD1 (PDB code: 2v1d). Upper panel: Superimposed conformation of compound 29 (green) and FAD (yellow) within the active site of LSD1. Lower panel: Interactions between compound 29 (beige) and key amino acid residues (green) surrounding the LSD1 binding pocket (LSD1 protein in light pink). Hydrogen bonds are shown in sky blue, while H–π and π–π interactions are shown in orange.

LSD1 inhibition enhances the anti-tumor immune activity of macrophages and CD8$^+$ T cells.

To determine the regulatory effectiveness of KL-1 targeting LSD1 on modulating macrophage and CD8$^+$ T-cell responses within the GC microenvironment, *in vitro* co-incubation experiments were performed. Macrophages exposed to CM derived from KL-1-treated GC cells exhibited a concentration-dependent increase in pro-inflammatory M1 markers (CD80, CD86) and a concomitant reduction in immunosuppressive M2 markers (CD206, CD163) (Fig. 5, A, B; Fig. S4A, B), indicating that LSD1 inhibition reprograms M0 macrophages toward a pro-inflammatory M1 phenotype. Similarly, T cells cultured with CM from GC cells treated with KL-1 showed elevated levels of activation markers CD69 and CD25 (Fig. 5C, D; Fig. S4C, D). To further evaluate the effect of LSD1 on CD8$^+$ T-cell exhaustion pathways, co-culture assays revealed that inhibiting LSD1 attenuated CD8$^+$ T-cell exhaustion by hindering the skewing of M0 macrophages toward the M2 phenotype (Fig. 5E-G). Simultaneously, the target specificity of KL-1 was verified (Fig. 5H). In conclusion, these findings reveal that targeting LSD1 in GC cells establishes an immunostimulatory microenvironment by simultaneously enhancing M1 macrophage polarization and CD8$^+$ T-cell activation, and concurrently alleviates CD8$^+$ T-cell exhaustion through the suppression of M0 macrophage polarization into M2.



347

348 **Fig. 5** LSD1 inhibition enhances the anti-tumor immune responses of macrophages and $CD8^+$

349 T cells. A and B Proportions of macrophages polarized to $CD86^+$ (A) and $CD80^+$ (B) phenotypes

350 after co-culture with the CM from AGS (left) and MKN45 cells (right) treated with KL-1. C and D

351 Flow cytometry was used to detect $CD8^+CD69^+$ (C) and $CD8^+CD25^+$ (D) T cells, after a 48-hour

352 co-culture with CM from KL-1-treated AGS cells. E-G Expression of LAG-3 (E), PD-1 (F), and

TIM-3 (G) after an 8-day co-culture with M2 macrophages pretreated with CM from KL-1-treated AGS and MKN45 cells. H Flow cytometry was used to detect CD80 expression on M0 macrophages following co-culture with CM, and TIM-3 expression on T cells after co-culture with CM-pretreated M2 macrophages. In all cases, the CM was sourced from DMSO/KL-1-treated control or LSD1-knockout MKN45 cells.

LSD1 inhibition suppresses GC growth by promoting the anti-tumor functions of macrophages and T cells.

To delineate the mechanistic involvement of macrophages and T lymphocytes in LSD1 inhibitor-mediated suppression of GC growth, a murine subcutaneous tumor model was established using MFC cells. Macrophage and $CD8^+$ T-cell populations were selectively depleted via anti-CSF1R and anti-CD8α prior to tumor inoculation. Treatment with the LSD1 inhibitor KL-1 significantly inhibited tumor growth (Fig. 6A-C), which was partially reversed by macrophage depletion and completely abolished upon $CD8^+$ T-cell depletion, indicating that the therapeutic effect relies predominantly on T cells, with an additional contribution from macrophages. Given the aforementioned findings that LSD1 suppresses M0 polarization into the M1 phenotype and $CD8^+$ T-cell activation while facilitating $CD8^+$ T-cell exhaustion through M2 macrophage-dependent pathways (Fig. 3), we assessed immune cell dynamics following KL-1 treatment. In the KL-1 + IgG group, LSD1 inhibition significantly increased $CD8^+$ T-cell enrichment (Fig. 6D; Fig. S5A), an effect that was lost upon macrophage depletion, suggesting that macrophages mediate LSD1-driven $CD8^+$ T-cell recruitment. KL-1 also promoted the abundance of M1 macrophages while suppressing

the frequency of M2 macrophages (Fig. 6E, F; Fig. S5B, C); however, these effects were abolished following $CD8^+$ T-cell depletion (Fig. 6E, F; Fig. S5B, C), implying that T cells are involved in the orchestration of LSD1-driven changes in M1 and M2 macrophage proportions. Immunohistochemical analyses further confirmed increased M1 and $CD8^+$ T-cell enrichment and decreased M2 accumulation in KL-1-treated tumors (Fig. 6G). Hematoxylin and eosin staining revealed no *in vivo* toxicity by KL-1 (Fig. S5D). Collectively, these findings reveal that LSD1 inhibitor KL-1 orchestrates anti-tumor immunity through crosstalk between macrophages and $CD8^+$ T cells, enhancing M1 phenotype and $CD8^+$ T-cell activation while suppressing M2-mediated $CD8^+$ T-cell exhaustion, thereby positioning KL-1 as a promising therapeutic candidate for GC therapy.

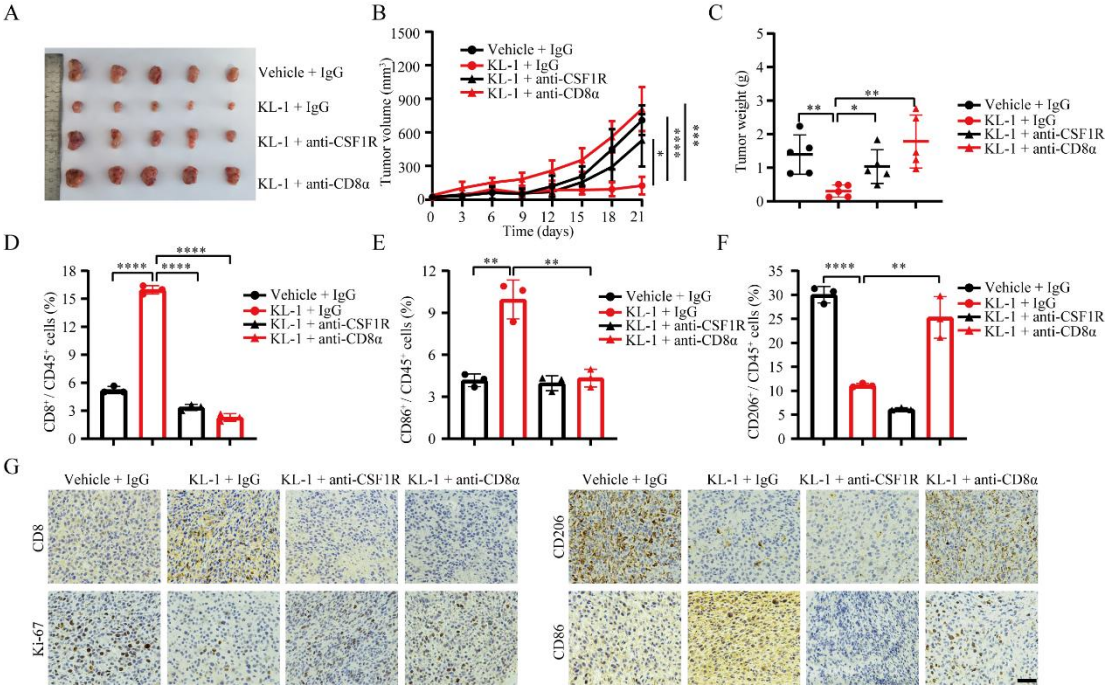


Fig. 6 LSD1 inhibition suppresses GC growth by promoting the anti-tumor responses of macrophages and $CD8^+$ T cells. A-C Tumor images (A), tumor growth curves (B), and tumor weights (C) of 615 mice bearing MFC cells following macrophage and $CD8^+$ T-cell depletion. The

data are shown as the mean ± SD; $n = 5$. D-F Flow cytometry analyzed the frequency of $CD8^+$ T cells(D), $CD86^+$ macrophages(E), and $CD206^+$ macrophages (F) in tumors from 615 mice bearing MFC CON or MFC LSD1 KO cells. Data are represented as the mean ± SD; $n = 3$; two-tailed unpaired Student's *t*-test; $^{****}p < 0.0001$, $^{**}p < 0.01$. G Immunohistochemical analysis of CD8, CD206, CD80, and Ki-67 in tumor tissues of 615 mice. Scale bar, 300 μm.

Discussion

LSD1 exerts multifaceted functions in shaping the tumor immune microenvironment of GC, involving epigenetic modifications, immune cell infiltration, and tumor progression[37, 38]. Despite the established role of LSD1 in cancer immunomodulation[39-42], little is known about its precise role in the local immune microenvironment of GC. In this study, through integrated scRNA-seq, murine models, and *in vitro* assays, we revealed that LSD1 exerts dual immunosuppressive functions: it suppresses macrophage polarization toward pro-inflammatory M1 phenotypes and $CD8^+$ T-cell activation, while simultaneously facilitating $CD8^+$ T-cell exhaustion through driving macrophage differentiation into pro-tumorigenic M2 phenotypes. The inhibition of LSD1 using KL-1 reversed this immunosuppressive program by reprogramming macrophage polarization and restoring $CD8^+$ T-cell responses, ultimately impairing tumor growth. These findings establish a novel understanding of the immune-mediated mechanisms responsible for the anti-cancer effect of LSD1 blockade and highlight the promise of LSD1 inhibition as a potential therapeutic approach for GC.

This study has limitations, including the absence of GC patient scRNA-seq data

and *in vivo* validation of the LSD1–M2–$CD8^+$ T-cell exhaustion axis. Future work will involve profiling clinical samples with differential LSD1 expression and employing OT-I mice to clarify causality.

The elevated expression of LSD1 is strongly linked to adverse prognosis in multiple malignancies[43-45], likely due to its role in driving epithelial-mesenchymal transition (EMT), cellular differentiation, invasion and immune evasion[46, 47]. While the impact of LSD1 on T-cell responses has been reported[48-50], its specific relationship with $CD8^+$ T-cell exhaustion was previously uncharacterized. Our data provide initial proof that LSD1 promotes $CD8^+$ T-cell exhaustion by driving the shift of M0 macrophages into the pro-cancer M2 phenotype. Importantly, $CD8^+$ T-cell depletion abolished LSD1-driven M1/M2 macrophage shifts (Fig. 3H; Fig. S3I and J; Fig. 6E and F), suggesting that T cells are involved in the regulation of macrophage phenotypes by LSD1.These findings suggest that LSD1 may orchestrate macrophage–T cell crosstalk, consistent with previous reports highlighting reciprocal interactions between these immune populations[34, 51-53]. Further mechanistic investigation is warranted to elucidate how LSD1 governs this interplay, which may inform the development of LSD1-targeted combination immunotherapies for GC.

Materials and methods

Cell cultures

Human GC cell lines (AGS and MKN45), THP-1 cell lines, RAW264.7 cells, and mouse GC cells (MFC) were obtained from the National Cell Resource Center. Cell lines were authenticated using short tandem repeat (STR). AGS, MKN45, THP-1, and

MFC cell lines were cultured in Roswell Park Memorial Institute 1640 medium (RPMI 1640; C3010-0500, BI, Israel) containing 10% (v/v) fetal bovine serum (FBS) (C04001-500, BI, Israel). RAW264.7 cells were maintained in Dulbecco's Modified Eagle Medium (C3110-0500, BI, Israel) supplemented with 10% FBS. Each cell line in this study was grown at 37°C in a humidified environment containing 5% CO_2.

Animal studies

Five- to six-week-old 615 mice were sourced from the Institute of Hematology at the Chinese Academy of Medical Sciences. Upon arrival, all animals underwent a seven-day adaptation period in pathogen-free housing conditions prior to experimental procedures. Mice were distributed into experimental cohorts at random and received subcutaneous injections of either MFC CON or MFC LSD1 KO cells (6×10^5 cells per mouse). All animal studies obtained approval from the Ethics Committee of Zhengzhou University (Approval No. 23-IACUC-y125, 24-IACUC-y074, 24-IACUC-y144).

To deplete $CD8^+$ T cells, anti-CD8α (200 μg/mouse) (A2102, Selleck, China) were administered intravenously every other day, starting 48 hours before cancer cell inoculation and continuing until the experiment endpoint. Macrophage depletion was achieved using three distinct methods. In the first protocol, clodronate liposomes (100 μL/mouse; 40337ES10, Liposomes, Netherlands) were administered intraperitoneally, while control mice received control liposomes (100 μL/mouse; 40338ES10, Liposomes, Netherlands) treatment. The second approach utilized PLX3397 (400 mg/kg; HY-16749, MCE, USA), with vehicle solvent serving as control. The third strategy involved anti-CSF1R (300 μg/mouse; A2159, Selleck, China), with IgG isotype antibodies as control.

All macrophage depletion regimens began 48 hours prior to tumor cell inoculation and were administered intraperitoneally every other day until the experimental endpoint. For combination depletion, mice were co-treated with anti-CD8α and anti-CSF1R, while control animals received IgG isotype antibodies. At the experimental endpoint, mice were euthanized following humane protocols. Then, tumors were harvested for subsequent flow cytometry and histopathological analyses.

For KL-1 treatment in the subcutaneous tumor model, 615 mice were randomly assigned to four groups: vehicle + IgG, KL-1 + IgG, KL-1 + anti-CSF1R, and KL-1 + anti-CD8α. To establish selective immune cell depletion, mice in the relevant groups received tail vein intravenous injections of anti-CSF1R or anti-CD8α starting two days before the subcutaneous implantation of MFC tumor cells (6×10^5 cells/mouse). Antibody administration continued every other day post-implantation to sustain macrophage or $CD8^+$ T-cell depletion. Once tumors were established, KL-1 (50 mg/kg) was administered by intragastric gavage every other day. At the experimental endpoint, mice were humanely euthanized, and tumors were surgically removed for downstream analyses.

Establishment of LSD1 knockout GC cells

GC cells were maintained in 96-well plates. Following cell adherence and reaching approximately 30% confluence, the cells were infected with a lentivirus (Genechem, Shanghai, China) encoding the CRISPR/Cas9 construct targeting the LSD1 gene. Following 12 hours of infection, the viral supernatant was substituted with fresh complete medium. Once cells reached full confluence, single-cell clones were obtained

through limiting dilution and individually expanded. The efficiency of LSD1 knockout in the resulting clones was validated by western blot analysis. The sgRNA sequences used for LSD1 knockout were as follows: human, 5′-CCGGCCCTACTGTCGTGCCT-3′; mouse, 5′-CCTGAGAGGTCATTCGGTCA-3′.

Western blot

Cells were subjected to lysis on ice for 30 minutes using RIPA buffer with a protease inhibitor cocktail (A8260, Solarbio, China), followed by collected the supernatant. Then, quantification using a BCA assay kit (PC0020, Solarbio, China). Following the addition of loading buffer, proteins underwent heat denaturation prior to SDS-PAGE separation. Subsequently, nitrocellulose (NC) membranes (66485, Pall, USA) were used to transfer the separated proteins. Following treatment for 2 hours using 5% skim milk in PBST at ambient temperature, anti-LSD1 (ab129195, Abcam, USA) and anti-GAPDH (511203, Zenbio, China) were used to incubate for 12 hours with membranes at 4°C. After washing completion with PBST (10 minutes each), membranes were treated for 2 hours with horseradish peroxidase-conjugated secondary antibodies (ZB-2301, Zsbio, China) at ambient temperature. Following four additional washes with PBST, immunoreactive signals were detected by enhanced chemiluminescence, and the images were captured with a chemiluminescence imaging system.

Separation of $CD45^+$ cells in mouse tumor tissues

Mouse tumor tissues were processed to isolate $CD45^+$ cells using the MagniSort™ Mouse CD45 Positive Selection Kit (8802-6865-74, Thermo Fisher, USA). In detail,

tumor tissues from 615 mice were sectioned into pieces of 2-4 mm and subjected to enzymatic digestion with hyaluronidase (H3506, Sigma, USA) and collagenase IV (LS004188, Thermo Fisher, USA). The digested tissues were subsequently filtered to eliminate cellular clumps. The remaining cellular suspension was centrifuged and resuspended in PBS containing 3% FBS and 10 mM ethylenediaminetetraacetic acid (separation buffer), forming a suspension of single cells at a density of 1×10^8 cells per mL. Subsequently, the suspension was combined with MagniSort^{TM} Anti-Mouse CD45 Biotin B at ambient temperature for 10 minutes. The cells were subjected to washing and resuspension in separation buffer. MagniSort^{TM} Positive Selection Beads A were then introduced to the sample, after which it underwent a further 10-minute incubation at ambient temperature. The samples were then adjusted to the final volume of 2.5mL using separation buffer and placed for 5 minutes in a magnetic rack. The cell pellets were resuspended in isolation solution after discarding the supernatant for further experiments.

Single-cell sequencing

Initially, the count and viability of sorted $CD45^+$ cells were assessed using a fluorescence cell analyzer (Countstar Rigel S2, Countstar, China) in combination with acridine orange (CA1143, Solarbio, China) and propidium iodide (C0080, Solarbio, China) staining reagents. Subsequently, cells were washed twice using RPMI 1640 and resuspended in PBS containing 0.04% FBS at a final density of 1×10^6 cells/mL. Following this, scRNA-seq and TCR libraries were constructed utilizing the Chromium Next GEM Single Cell 5' Kit v2 (16 rxns PN-1000263, 10× Genomics, USA) following

the manufacturer's instructions. The resulting libraries were purified and quantified using a Qubit (EQ121-01, Vazyme Biotech, China) and their quality was examined on an Agilent 2100 Bioanalyzer instrument (Agilent Technologies, USA). The illumina NovaSeq 6000 platform (Illumina, USA) was used to sequence 150-bp paired-end reads. The paired-end reads were trimmed to 26 bp (R1) and 98 bp (R2) using Cutadapt version 3.4[54], while quality control of sequencing data was assessed by FastQC version 0.11.9[55]. TCR clonotype diversity was evaluated with the vegan R package (v2.5-7)[56].

Immunofluorescence staining (IF)

Mouse spleens and tumor tissues underwent processing through a standard series of paraformaldehyde fixation and ethanol dehydration, followed by sectioning and antigen retrieval. Following preparation, the sections were subjected to a 12-hour incubation at 4 °C in primary antibodies including anti-F4/80 (ab111101, Abcam, USA), anti-CD206 (24595T, CST, USA), and anti-CD86 (ER1906-01, HuaBio, China). Fluorescent secondary antibodies (A24221, Abbkine, China) were then applied, followed by DAPI (HY-D1738, MCE, USA) staining to visualize nuclei for 10 minutes. The samples were visualized using a Nikon C2 Plus confocal microscope (Nikon, Japan).

Detection of M1 and M2 macrophages using flow cytometry

GC cells were plated and adhered in six-well culture dishes, followed by replacement of the medium with fresh culture medium. CM was collected 24 hours later. THP-1 cells were plated in six-well plates and induced to differentiate into macrophages

using PMA (HY-18739, MCE, USA) for 48 hours. The resulting macrophages were then treated with CM from AGS and MKN45 GC cells with or without LSD1 knockout. After treatment completion, macrophages were harvested and stained for 30 minutes with the following antibodies: APC/Cy7-anti-CD206(321120, Biolegend, USA), PE-anti-CD206 (141706, Biolegend, USA), PE-anti-CD163 (12-1639-42, Thermo Fisher, USA), FITC-anti-CD86 (374204, Biolegend, USA), and PE-anti-CD80 (305208, Biolegend, USA). Similarly, RAW264.7 cells underwent treatment with CM for 48 hours, followed by assessment of CD206 expression. Flow cytometry (FACSCalibur, BD, USA) was conducted to evaluate the expression of CD163, CD206, CD86, and CD80.

Macrophage polarization *in vitro*

Macrophage polarization was performed according to established protocols. Briefly, THP-1 cells were initially stimulated for 48 hours with phorbol 12-myristate 13-acetate (PMA, 100 ng/mL; 16561-29-8, MCE, USA) to induce naïve macrophages (M0). M0 macrophages were then polarized into the M1 phenotype through a 48-hour stimulation with IL-2 (20 ng/mL; GMP-11848-HNAE, SinoBiological, China) combined with LPS (100 ng/mL; HY-D1056, MCE, USA). For M2 polarization, parallel cultures of M0 macrophages were additionally activated using 20 ng/mL each of IL-4 (11846-HNAE, SinoBiological, China) and IL-13 (HY-P7033, MCE, USA) for an equivalent duration of 48 hours.

Macrophage migration assays

LSD1 knockout and control AGS and MKN45 cells were plated into 24-well

culture dishes. Following cell adhesion, THP-1 cells differentiated into M1 and M2 macrophages were placed in the upper chamber and co-cultured with AGS or MKN45 cells at 37°C for 24 hours. After fixation with 4% paraformaldehyde, migrated cells were subjected to nuclear staining using DAPI (HY-D1738, MCE, USA). Cell migration was determined by quantifying the cell count in three randomly chosen microscopic fields per insert.

Peripheral blood mononuclear cell separation

Blood samples were harvested from healthy individuals for the isolation of peripheral blood mononuclear cells (PBMCs) using lymphocyte isolation medium (LTS1077, TBD, China) as per the manufacturer's guidelines. PBMCs were subsequently cultured in RPMI 1640 medium containing 10% FBS in a 5% CO_2 environment at 37°C. These cells were subjected to a stimulation with anti-CD3/CD28 beads (10971, Stemcell, Canada) for 72 hours under the same culture conditions to activate T cells.

Co-incubation experiment

$CD8^+$ T-cell activation was evaluated by co-incubating T cells with tumor cell-derived CM for 48 hours, followed by flow cytometry was used to analyze the expression of CD69 and CD25.

For the $CD8^+$ T-cell exhaustion experiments, T cells were co-incubated for 8 days with CM derived from control, LSD1 knockout tumor cells, or KL-1-treated tumor cells, after which flow cytometry was employed to assess the expression of LAG-3, PD-1, and TIM-3. During the incubation period, the CM was replaced every 24 hours.

In the macrophage-T cell co-incubation experiments, THP-1 cells were first induced into M2 macrophages and subsequently treated for 48 hours with CM derived from control or LSD1 knockout tumor cells and KL-1-treated tumor cells. These M2 macrophages were then co-cultured with T cells for a further 8 days supplemented with IL-2 (GMP-11848-HNAE, SinoBiological, China) and anti-CD3/CD28 (10971, Stemcell, Canada). Subsequently, T cells were incubated with an antibody cocktail consisting of FITC-anti-CD45 (304006, Biolegend, USA), APC-anti-CD3 (300312, Biolegend, USA), PerCP/Cyanine5.5-anti-CD8 (301031, Biolegend, USA) and PE-anti-LAG-3 (36930, Biolegend, USA)/PE-anti-PD-1 (379210, Biolegend, USA)/PE-anti-TIM-3 (364806, Biolegend, USA). Flow cytometry was utilized to evaluate the frequency of CD8 T_{ex}.

Tumor-infiltrating leukocyte detection by flow cytometry

Tumor tissues from 615 mice were minced with ophthalmic scissors and then digested at 37°C for 2 hours using collagenase and hyaluronidase to obtain single-cell suspensions. For T-cell analysis, samples were exposed to an antibody cocktail targeting CD45 (103116, Biolegend, USA), CD3 (100236, Biolegend, USA), and CD8 (100708, Biolegend, USA). For macrophage analysis, samples were stained on ice for 30 minutes using an antibody cocktail targeting F4/80 (123108, Biolegend, USA), CD86 (10501, Biolegend, USA)/CD206 (141708, Biolegend, USA). Flow cytometry was conducted on a BD FACSCanto flow cytometer (BD Biosciences, USA) to identify $CD8^+$ T cells, $F4/80^+CD86^+$ macrophages, and $F4/80^+CD206^+$ macrophage populations in mouse tumor tissues. The data were evaluated using the FlowJo software (version 10.4, BD,

USA).

Immunohistochemistry experiments (IHC)

Tumor tissues from mice were immersed in 4% paraformaldehyde and then embedded in paraffin. Following sectioning at a thickness of 4 μm, tissue samples were deparaffinized in xylene and rehydrated in graded alcohol concentrations (75%, 85%, 95%, and 100%). The slides were subsequently treated with antigen retrieval using 1 mM Tris/EDTA buffer (pH 9.0). After blocking with 5% goat serum, samples were treated overnight with primary anti-Ki-67 (ab16667, Abcam, USA), anti-CD8α (50389-T26, SinoBiological, China), anti-CD86 (ER1906-01, HuaBio, China), and anti-CD206 (24595T, CST, USA) at 4°C. After washing, sections underwent a 2-hour incubation at 37°C using a peroxidase-conjugated secondary antibody (ZB-2301, Zsbio, China), followed by staining with DAB substrate (ZLI9018, ZSGB-Bio, China). Stained samples were imaged using the Aperio AT2 scanner (Leica Biosystems, Germany).

H&E staining

Upon completion of the animal experiments, mice were euthanized and subjected to surgical harvest of cardiac, hepatic, splenic, pulmonary, and renal tissues. Freshly collected organs were treated with 4% paraformaldehyde at ambient temperature for 48 hours. The fixed specimens were subsequently dehydrated with a range of ethanol concentrations (75%, 85%, 95%, 100%, and 100%), cleared in xylene, and infiltrated with paraffin. Following sectioning at a thickness of 4 μm, paraffin-embedded tissues were dewaxed by three 10-minute xylene treatments and rehydrated through a descending ethanol gradient (100%, 100%, 95%, 85%, 75%) with 5-minute incubations

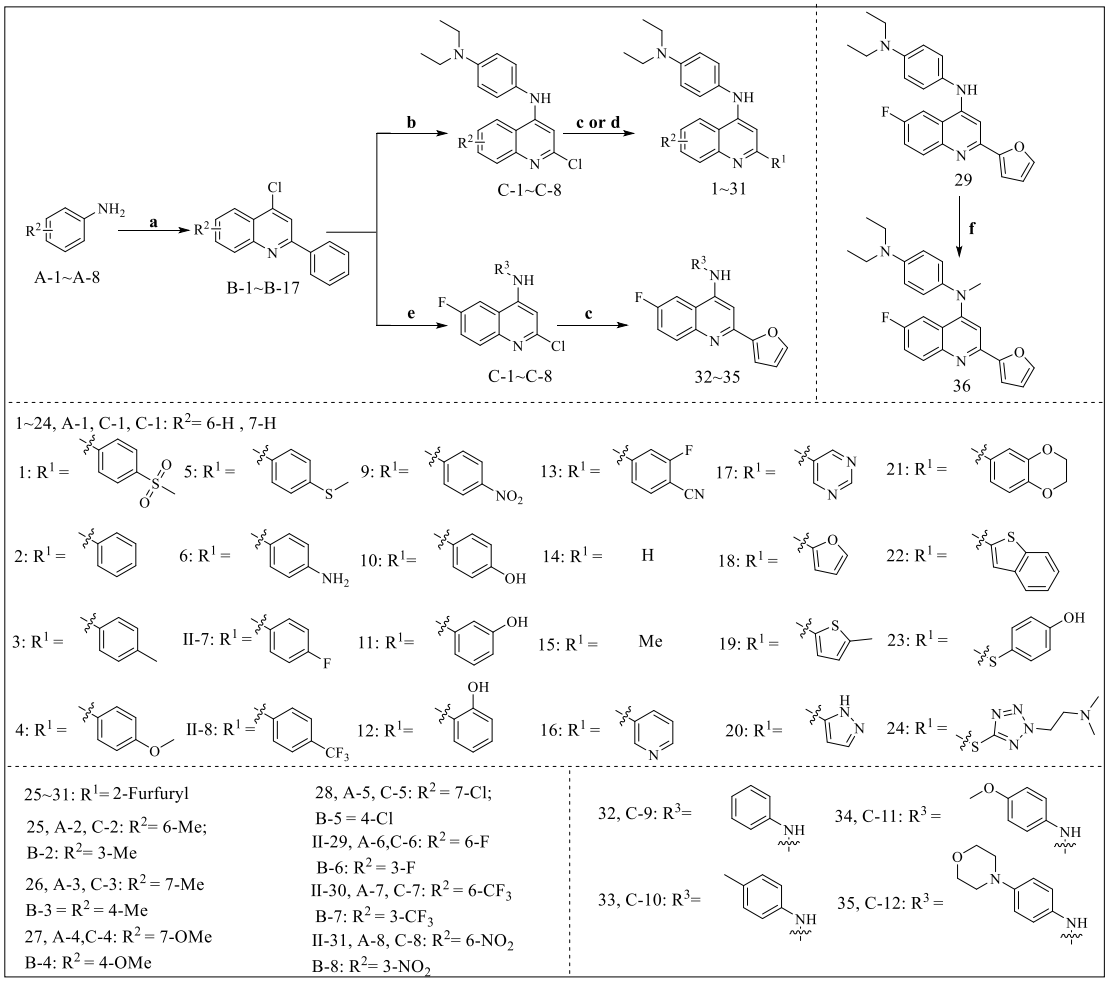
at each concentration. After rinsing in water, nuclear staining was performed with hematoxylin (BA4097, BASO, China) for 1 minute, followed by differentiation in 1% acid-alcohol and rinsed in running tap water. Counterstaining was achieved with eosin Y solution (BA4098, BASO, China) for 10 minutes, and then dehydration was performed through an ascending alcohol concentration (75%, 85%, 95%, 100%, 100%; 5 minutes each) and clearing in xylene (3 × 10 minutes). Finally, sections were permanently mounted with neutral balsam under coverslips and air-dried prior to imaging using brightfield microscopy with standardized magnification settings.

General information for Chemistry

Commercial reagents and solvents were employed without additional purification. Target compounds were subjected to a purification using silica gel column chromatography (200–300 mesh). An X-5 micro melting point apparatus was used to measure the melting points. A Bruker spectrometer (400 MHz) in $CDCl_3$ or DMSO-d_6 with TMS as an internal standard was employed to record the ^{1}HNMR spectra. High-resolution mass spectra (HRMS) were recorded using an Agilent 6545 Q-TOF LC/MS instrument in ESI mode, except for compounds 8 and 34, which were analyzed with a Thermo Fisher Q Exactive™ Plus mass spectrometer. HPLC analysis (Agilent 1260 system with a Zorbax SB-C18 column, 5 μm, 150 mm × 4.6 mm) confirmed that all final compounds had a purity greater than 95%. A 10-minute linear gradient elution using water (A) and methanol (B) was performed, transitioning from 90:10 to 0:100 (A/B, v/v) at a flow rate of 1 mL/min, with detection at 254 nm.

Synthesis of target compounds 1–36

A synthetic route was designed to construct novel 2-amino-4-arylquinoline-based LSD1 inhibitors, as outlined in Scheme 1. Aniline (intermediate A-1) was reacted with malonic acid using phosphorus oxychloride to produce intermediate B-1. Intermediate B-1 was then condensed with N,N-diethyl-1,4-phenylenediamine to form intermediate C-1. Subsequent Suzuki coupling of C-1 with aryl or heteroaryl boronic acids using potassium carbonate and Pd(P(tBu)3)2 catalyst afforded the target compounds 1 to 22. Additionally, C-1 was reacted with *p*-mercaptophenol or 1-(2-dimethylaminoethyl)-1H-5-mercaptotetrazole in the presence of DIPEA to generate compounds 23 and 24. Similarly, substituted anilines were reacted with malonic acid to obtain intermediates A-2–A-8, which were then condensed with N,N-diethyl-1,4-phenylenediamine to yield intermediates B-2–B-8. These underwent Suzuki coupling with 2-furylboronic acid to afford compounds 25–31. Furthermore, intermediate B-6 was reacted with substituted anilines under concentrated hydrochloric acid to form intermediates C-1–C-8, which were coupled with 2-furylboronic acid to obtain compounds 32 to 35. Lastly, compound 29 was methylated with methyl iodide under basic conditions to generate the target product 36.



Scheme 1 Synthesis of target compounds 1–36. (a) Succinic acid, phosphorus oxychloride, 1,4-dioxane, 80 ℃, 5 h; (b) Concentrated hydrochloric acid, isopropanol, 75 ℃, 8 h; (c) Potassium carbonate, bis(tri-tert-butylphosphine)palladium, $V_{1,4\text{-dioxane}}$: V_{water} = 4:1, nitrogen, 100℃, 6 h; (d) *N,N*-dipropylamine, *N,N*-dimethylformamide, 90 ℃, 7 h; (e) Bis(trimethylsilyl)ammonium potassium, tetrahydrofuran, nitrogen, 65℃, 10 h; (f) Methyl iodide, sodium hydride, *N,N*-dimethylformamide, 0°C, 3 h.

Synthesis of compounds 1–22

Compound A-1 (10 mmol) and malonic acid (11 mmol) were solubilized in 50 mL of 1,4-dioxane. The mixture was reacted for 4 hours at 80°C, and thin-layer chromatography (TLC) was conducted to track the progress. After reaching room

temperature, the resulting solution was treated with a dropwise addition of phosphorus oxychloride (20 mmol) with stirring, and the progress was tracked by TLC. The solution was then quenched by slowly pouring it into an ice-water mixture with agitation for 30 minutes. The resulting mixture underwent five extractions using 50 mL solution of ethyl acetate and then washed with saturated sodium chloride. Following drying over anhydrous sodium sulfate and filtration, the organic phases were subjected to evaporation using a rotary evaporator. The resulting compound was treated using column chromatography for purification to yield intermediate B-1. Intermediate B-1 (10 mmol) and N,N-diethyl-p-phenylenediamine (12 mmol) were added sequentially to 50 mL of isopropanol. Under stirring at 70°C, the reaction proceeded for 8 hours following the dropwise addition of 3 mL of concentrated hydrochloric acid. The whole progress was tracked by TLC. After finished, the solution underwent three extractions using 50 mL of ethyl acetate and then washed with saturated sodium chloride. After drying over anhydrous sodium sulfate and filtration, the combined organic layer was subjected to concentration in the condition of reduced pressure. The resulting products were processed through column chromatography for purification, yielding intermediate C-1. Intermediate C-1 (0.5 mmol) and various boronic acids (0.75 mmol) were introduced into a 20 mL solution of water and 1,4-dioxane ($V_{1,4\text{-dioxane}}$: V_{water} = 4:1). After the addition of potassium carbonate (0.875 mmol) and bis(tri-tert-butylphosphine)palladium (0.025 mmol), the reaction was conducted at 100°C in the presence of nitrogen for 8 hours with stirring, and TLC was used to monitor the whole progress. Subsequently, the resulting solution was subjected to three extractions using

a 20 mL solution of ethyl acetate and then washed with saturated sodium chloride. Following drying over anhydrous sodium sulfate and filtration, the combined organic extracts underwent a concentration in the condition of reduced pressure. After completion, these crude products were processed using column chromatography for purification to obtain compounds 1–22.

Synthesis of compounds 23–24

Intermediate C-1 (0.5 mmol) and thiol compounds (0.75 mmol) were solubilized in 20 mL of N,N-dimethylformamide (DMF), after which N,N-diisopropylethylamine (0.75 mmol) was introduced. With stirring at 90°C, the reaction proceeded for 7 hours, with progress monitored via TLC. Subsequently, the resulting solution was subjected to three extractions with 20 mL dichloromethane/20 mL saturated sodium chloride. Following drying over anhydrous sodium sulfate and filtration, the resulting organic phases were treated with a rotary evaporator for concentration. The crude products underwent column chromatography to obtain compounds 23–24.

Synthesis of Compounds 25–31

Compounds A-2 to A-8 (10 mmol) and malonic acid (11 mmol) were dissolved in 40 mL of 1,4-dioxane and reacted for 4 hours at 80°C, monitored by TLC. After being cooled to ambient temperature, the solution was gradually introduced into phosphorus oxychloride (20 mmol) under stirring, with the progress tracked using TLC until completion. Following the quenching of the reaction in 100 mL of an ice-water mixture with 30 minutes of stirring, the resulting mixture was subjected to five extractions with 50 mL solution of ethyl acetate and then washed with saturated sodium chloride.

Following drying over anhydrous sodium sulfate and filtration, the organic solvent underwent evaporation in the condition of reduced pressure. Purification by column chromatography of the crude mixture afforded intermediates B-2–B-8. Intermediates B-2–B-8 (10 mmol) and N,N-diethyl-p-phenylenediamine (12 mmol) were sequentially added to 100 mL of isopropanol. Under stirring at 70°C, the reaction was continued for 8 hours following the dropwise addition of 3 mL of concentrated hydrochloric acid and monitored by TLC. The resulting solution underwent three extractions using a 50 mL mixed solution of ethyl acetate and then washed with saturated sodium chloride. Following drying over anhydrous sodium sulfate and filtration, the organic phases were evaporated using a rotary evaporator. The crude products were processed through column chromatography for purification to yield intermediates C-2–C-8. 1 mmol Intermediates C-2–C-8 and 1.25 mmol 2-furanboronic acid were subsequently dissolved in a 20 mL mixed solution of water and 1,4-dioxane ($V_{1,4\text{-dioxane}} : V_{water} = 4:1$). Potassium carbonate (1.75 mmol) and bis(tri-tert-butylphosphine)palladium (0.05 mmol) were then sequentially added. Stirring at 70°C, the reaction continued for 8 hours in the presence of nitrogen, and the progress was tracked by TLC. The resulting solution was exposed to 20 mL ethyl acetate for three extractions and then washed with saturated sodium chloride. Following drying with anhydrous sodium sulfate and filtration, the combined organic phases were concentrated in the condition of reduced pressure. Subsequently, purification by column chromatography furnished compounds 25–31.

Synthesis of compounds 32–35

Potassium bis(trimethylsilyl)amide (12 mmol) and various anilines (12 mmol)

were sequentially added to 50 mL of tetrahydrofuran, followed by 30-minute stirring under nitrogen at ambient temperature. After the addition of intermediate B-6 (10 mmol) into the mixture, reaction was continued for 10 hours at 70°C in the presence of nitrogen with stirring, and monitored by TLC. The solution underwent three extractions using a 50 mL mixture of ethyl acetate and then washed with saturated sodium chloride. Following drying over anhydrous sodium sulfate and filtration, the organic phases were subjected to evaporation using a rotary evaporator. Subsequently, purification by column chromatography furnished intermediates C-9 to C-12. Intermediates C-9 to C-12 (1 mmol) and 2-furanboronic acid (1.25 mmol) were solubilized in a 20 mL solution of water and 1,4-dioxane ($V_{1,4\text{-dioxane}}$: V_{water} = 4:1). Following the addition of potassium carbonate (1.75 mmol) and bis(tri-tert-butylphosphine)palladium (0.05 mmol), the reaction was conducted for 8 hours at 100°C under a nitrogen atmosphere with stirring, monitored using TLC. The solution underwent three extractions using a 20 mL solution of ethyl acetate and subsequently washed with saturated sodium chloride. Following drying over anhydrous sodium sulfate and filtration, the resulting organic phases were treated using a rotary evaporator for evaporation, after which purification by column chromatography furnished compounds 32–35.

Synthesis of compound 36

Intermediate 29 (0.5 mmol) and sodium hydride (0.6 mmol) were introduced into 10 mL of tetrahydrofuran. Then, the resulting mixture was maintained in an ice bath for half an hour, and the whole process was tracked by TLC, followed by dropwise addition of iodomethane (0.5 mmol). The resulting solution underwent three extractions with 10

mL dichloromethane and subsequently washed with saturated sodium chloride. After finished, the resulting organic solvent underwent evaporation using a rotary evaporator to obtain compound 36.

Molecular docking

Molecular docking simulations were conducted using MOE 2015.10. The LSD1 crystal structure (PDB: 2V1D) was sourced from the Protein Data Bank and prepared by removing water molecules, followed by protonation and structural correction with the QuickPrep module. The Amber 10:EHT force field was used for energy minimization calculations. Compounds 1 and KL-1 were prepared through protonation and energy minimization, then docked against the LSD1 binding pocket using the standard Dock protocol. Binding affinities were assessed using the London dG and GBVI/WSA dG scoring functions.

Statistical analysis

GraphPad Prism software version 9.0 (GraphPad Company, USA) was employed to process all data. Data are shown as mean ± standard deviation (SD). Statistical tests employed for all quantitative data are provided in the figure legends. The quantification of migrating cells was assessed using ImageJ software (National Institutes of Health, USA). In this study, a p-value lower than 0.05 was regarded as statistically significant. n.s.: no significance; $****p < 0.0001$, $***p < 0.001$, $**p < 0.01$, $*p < 0.05$.

Declaration of interests

No competing interests are declared by the authors.

Contributors

Jing-Ru Pang carried out the majority of the experimental work and was responsible for data analysis, with assistance from Yu Zhang, Hao-Yi Zhu, Dan-Dan Shen, Bo Wang, who also contributed to methodology development, validation, and resource acquisition. Xing-Jie Dai, Yi-Chao Zheng and Hong-Min Liu designed and supervised the project, provided critical resources and technical support, and critically revised the manuscript. Zhenghong Yang, Xing-Jie Dai, Yi-Chao Zheng and Hong-Min Liu secured funding. All authors discussed the results, participated in data review, and provided their final approval of the version to be published.

Acknowledgments

The authors gratefully acknowledge Wuhan Frasergen Bioinformatics Co. Ltd for providing technical support in scRNA-seq. This work was supported by National Natural Science Foundation of China (No. 22477114 to YCZ; No. 82204213 to Xing-Jie Dai; No. U21A20416 and 82020108030 to HML, China); R&D of Key Project of Henan Province (No. 241111312500 to YCZ, China); Basic Research of the Key Project of the Higher Education from the Education Department of Henan Province (No. 22ZX008 to YCZ, China); the Young Top Talent Program from Henan Association for Science and Technology; the Natural Science Foundation of Henan Province (No. 252300421127 to Xing-Jie Dai, China); the Science and Technology R&D Program of Henan Province (No. 242102311195 to Zhenghong Yang, China).

Data availability

All data supporting these findings in this study are available in the article and

supplementary information. The raw scRNA-seq data in our work have been archived in the NCBI Sequence Read Archive (SRA), hosted under BioProject accession number PRJNA1354195.

References

1 Bray F, Laversanne M, Sung H, Ferlay J, Siegel R L, Soerjomataram I, et al. Global cancer statistics 2022: GLOBOCAN estimates of incidence and mortality worldwide for 36 cancers in 185 countries. CA Cancer J Clin. 2024; 74: 229-263.

2 Smyth E C, Nilsson M, Grabsch H I, van Grieken N C, Lordick F. Gastric cancer. Lancet. 2020; 396: 635-648.

3 Li K, Zhang A, Li X, Zhang H, Zhao L. Advances in clinical immunotherapy for gastric cancer. Biochim Biophys Acta Rev Cancer. 2021; 1876: 188615.

4 Yasuda T, Wang Y A. Gastric cancer immunosuppressive microenvironment heterogeneity: implications for therapy development. Trends in Cancer. 2024; 10: 627-642.

5 Joshi S S, Badgwell B D. Current treatment and recent progress in gastric cancer. CA Cancer J Clin. 2021; 71: 264-279.

6 Liu G, Wang F, Feng Y, Tang H. Metformin Inhibits NLRP3 Inflammasome Expression and Regulates Inflammatory Microenvironment to Delay the Progression of Colorectal Cancer. Recent Patents on Anti-Cancer Drug Discovery. 2025; 20: 213-222.

7 Liu G-L, Luo H, Liang D-D, Zhong L, Dai N, Lan W-H. Comprehensive Analysis of Prognostic Alternative Splicing Signatures in Tumor Immune Infiltration in Bladder Cancer. Recent Patents on Anti-Cancer Drug Discovery. 2025; 20: 185-199.

8 Shen D-D, Pang J-R, Bi Y-P, Zhao L-F, Li Y-R, Zhao L-J, et al. LSD1 deletion decreases exosomal PD-L1 and restores T-cell response in gastric cancer. Mol Cancer. 2022; 21: 75.

9 Zhang S, Liu M, Yao Y, Yu B, Liu H. Targeting LSD1 for acute myeloid leukemia (AML) treatment. Pharmacol Res. 2021; 164: 105335.

10 Sheng W, LaFleur M W, Nguyen T H, Chen S, Chakravarthy A, Conway J R, et al. LSD1 Ablation Stimulates Anti-tumor Immunity and Enables Checkpoint Blockade. Cell. 2018; 174.

11 Sehrawat A, Gao L, Wang Y, Bankhead A, McWeeney S K, King C J, et al. LSD1 activates a lethal prostate cancer gene network independently of its demethylase function. Proc Natl Acad Sci U S A. 2018; 115: E4179-E4188.

12 Schulte J H, Lim S, Schramm A, Friedrichs N, Koster J, Versteeg R, et al. Lysine-specific demethylase 1 is strongly expressed in poorly differentiated neuroblastoma: implications for therapy. Cancer Res. 2009; 69: 2065-2071.

13 Carmichael C L, Wang J, Nguyen T, Kolawole O, Benyoucef A, De Mazière C, et al. The EMT modulator SNAI1 contributes to AML pathogenesis via its interaction with LSD1. Blood. 2020; 136: 957-973.

14 Zhou X, Singh M, Sanz Santos G, Guerlavais V, Carvajal L A, Aivado M, et al. Pharmacologic Activation of p53 Triggers Viral Mimicry Response Thereby Abolishing Tumor Immune Evasion and Promoting Antitumor Immunity. Cancer Discov. 2021; 11: 3090-3105.

15 Tan A H Y, Tu W, McCuaig R, Hardy K, Donovan T, Tsimbalyuk S, et al. Lysine-Specific Histone Demethylase 1A Regulates Macrophage Polarization and Checkpoint Molecules in the Tumor Microenvironment of Triple-Negative Breast Cancer. Frontiers In Immunology. 2019; 10: 1351.

16 Bailey C P, Figueroa M, Gangadharan A, Lee D A, Chandra J. Scaffolding LSD1 Inhibitors Impair NK Cell Metabolism and Cytotoxic Function Through Depletion of Glutathione. Frontiers In Immunology. 2020; 11: 2196.

17 Wang Y, Liu Z, Li Y, Wang K, Yuan C, Shi J, et al. Peptide-based PET/CT imaging visualizes PD-L1-driven radioresistance in glioblastoma. Drug Resist Updat. 2025; 79: 101202.

18 Wang H, Wang X, Zhang X, Xu W. The promising role of tumor-associated macrophages in the treatment of cancer. Drug Resistance Updates. 2024; 73: 101041.

19 Yang L, Li A, Yu W, Wang H, Zhang L, Wang D, et al. Blockade of purine metabolism reverses macrophage immunosuppression and enhances anti-tumor immunity in non-small cell lung cancer. Drug Resistance Updates. 2025; 78: 101175.

20 Hatzi K, Geng H, Doane A S, Meydan C, LaRiviere R, Cardenas M, et al. Histone demethylase LSD1 is required for germinal center formation and BCL6-driven lymphomagenesis. Nat Immunol. 2019; 20: 86-96.

21 Qin Y, Vasilatos S N, Chen L, Wu H, Cao Z, Fu Y, et al. Inhibition of histone lysine-specific demethylase 1 elicits breast tumor immunity and enhances antitumor efficacy of immune checkpoint blockade. Oncogene. 2019; 38: 390-405.

22 Wu H, Liu J, Zhang X H, Jin S, Li P, Liu H, et al. The combination of flaxseed lignans and PD-1/PD-L1 inhibitor inhibits breast cancer growth via modulating gut microbiome and host immunity. Drug Resist Updat. 2025; 80: 101222.

23 Liu C, Liu L, Chen X, Cheng J, Zhang H, Zhang C, et al. LSD1 Stimulates Cancer-Associated Fibroblasts to Drive Notch3-Dependent Self-Renewal of Liver Cancer Stem-like Cells. Cancer Res. 2018; 78: 938-949.

24 Dai X J, Liu Y, Xiong X P, Xue L P, Zheng Y C, Liu H M. Tranylcypromine Based Lysine-Specific Demethylase 1 Inhibitor: Summary and Perspective. J Med Chem. 2020; 63: 14197-14215.

25 Liu H M, Zhou Y, Chen H X, Wu J W, Ji S K, Shen L, et al. LSD1 in drug discovery: From biological function to clinical application. Med Res Rev. 2024; 44: 833-866.

26 Dai X-J, Liu Y, Xue L-P, Xiong X-P, Zhou Y, Zheng Y-C, et al. Reversible Lysine Specific Demethylase 1 (LSD1) Inhibitors: A Promising Wrench to Impair LSD1. Journal of Medicinal Chemistry. 2021; 64: 2466-2488.

27 Sun K, Peng J D, Suo F Z, Zhang T, Fu Y D, Zheng Y C, et al. Discovery of tranylcypromine analogs with an acylhydrazone substituent as LSD1 inactivators: Design, synthesis and their biological evaluation.

28 Ishikawa Y, Gamo K, Yabuki M, Takagi S, Toyoshima K, Nakayama K, et al. A Novel LSD1 Inhibitor T-3775440 Disrupts GFI1B-Containing Complex Leading to Transdifferentiation and Impaired Growth of AML Cells. Mol Cancer Ther. 2017; 16: 273-284.

29 Duan Y, Qin W, Suo F, Zhai X, Guan Y, Wang X, et al. Design, synthesis and in vitro evaluation of stilbene derivatives as novel LSD1 inhibitors for AML therapy. Bioorg Med Chem. 2018; 26: 6000-6014.

30 Liu H M, Suo F Z, Li X B, You Y H, Lv C T, Zheng C X, et al. Discovery and synthesis of novel indole derivatives-containing 3-methylenedihydrofuran-2(3H)-one as irreversible LSD1 inhibitors. Eur J Med Chem. 2019; 175: 357-372.

31 Dai X J, Liu Y, Xue L P, Xiong X P, Zhou Y, Zheng Y A-O, et al. Reversible Lysine Specific Demethylase 1 (LSD1) Inhibitors: A Promising Wrench to Impair LSD1. J Med Chem. 2021; 64: 2466-2488.

898 32 Wang B, Wang S W, Zhou Y, Wang S P, Gao Y, Liu H M, et al. Discovery of 2-Aryl-4-
899 aminoquinazolin-Based LSD1 Inhibitors to Activate Immune Response in Gastric Cancer. Journal of
900 Medicinal Chemistry. 2024; 67: 16165-16184.
901 33 Waibl Polania J, Hoyt-Miggelbrink A, Tomaszewski W H, Wachsmuth L P, Lorrey S J, Wilkinson D
902 S, et al. Antigen presentation by tumor-associated macrophages drives T cells from a progenitor
903 exhaustion state to terminal exhaustion. Immunity. 2025; 58: 232-246.e236.
904 34 Kersten K, Hu K H, Combes A J, Samad B, Harwin T, Ray A, et al. Spatiotemporal co-dependency
905 between macrophages and exhausted CD8(+) T cells in cancer. Cancer Cell. 2022; 40: 624-638 e629.
906 35 Li Z, Ding L, Li Z, Wang Z, Suo F, Shen D, et al. Development of the triazole-fused pyrimidine
907 derivatives as highly potent and reversible inhibitors of histone lysine specific demethylase 1
908 (LSD1/KDM1A). Acta Pharm Sin B. 2019; 9: 794-808.
909 36 Kanouni T, Severin C, Cho R W, Yuen N Y, Xu J, Shi L, et al. Discovery of CC-90011: A Potent and
910 Selective Reversible Inhibitor of Lysine Specific Demethylase 1 (LSD1). J Med Chem. 2020; 63:
911 14522-14529.
912 37 Zhang B, Shi J, Shi X, Xu X, Gao L, Li S, et al. Development and evaluation of a human
913 CD47/HER2 bispecific antibody for Trastuzumab-resistant breast cancer immunotherapy. Drug Resist
914 Updat. 2024; 74: 101068.
915 38 Guo G, Zhou Z, Chen S, Cheng J, Wang Y, Lan T, et al. Characterization of the Prognosis and
916 Tumor Microenvironment of Cellular Senescence-related Genes through scRNA-seq and Bulk RNA-
917 seq Analysis in GC. Recent Pat Anticancer Drug Discov. 2024; 19: 530-542.

39 Yang Q, Wei S, Qiu C, Han C, Du Z, Wu N. KDM1A epigenetically enhances RAD51 expression to suppress the STING-associated anti-tumor immunity in esophageal squamous cell carcinoma. Cell Death & Disease. 2024; 15.

40 Sheng W, LaFleur M W, Nguyen T H, Chen S, Chakravarthy A, Conway J R, et al. LSD1 Ablation Stimulates Anti-tumor Immunity and Enables Checkpoint Blockade. Cell. 2018; 174: 549-563.e519.

41 Pallavicini I, Frasconi T M, Catozzi C, Ceccacci E, Tiberti S, Haas D, et al. LSD1 inhibition improves efficacy of adoptive T cell therapy by enhancing CD8+ T cell responsiveness. Nat Commun. 2024; 15.

42 Liu Y, Debo B, Li M, Shi Z, Sheng W, Shi Y. LSD1 inhibition sustains T cell invigoration with a durable response to PD-1 blockade. Nat Commun. 2021; 12.

43 Hosseini A, Dhall A, Ikonen N, Sikora N, Nguyen S, Shen Y, et al. Perturbing LSD1 and WNT rewires transcription to synergistically induce AML differentiation. Nature. 2025; 642: 508-518.

44 Prakasam R, Bonadiman A, Andreotti R, Zuccaro E, Dalfovo D, Marchioretti C, et al. LSD1/PRMT6-targeting gene therapy to attenuate androgen receptor toxic gain-of-function ameliorates spinobulbar muscular atrophy phenotypes in flies and mice. Nat Commun. 2023; 14: 603.

45 Li H, Wu B K, Kanchwala M, Cai J, Wang L, Xing C, et al. YAP/TAZ drives cell proliferation and tumour growth via a polyamine-eIF5A hypusination-LSD1 axis. Nat Cell Biol. 2022; 24: 373-383.

46 Boulding T, McCuaig R D, Tan A, Hardy K, Wu F, Dunn J, et al. LSD1 activation promotes inducible EMT programs and modulates the tumour microenvironment in breast cancer. Scientific Reports. 2018; 8.

938 47 Antona A, Leo G, Favero F, Varalda M, Venetucci J, Faletti S, et al. Targeting lysine-specific
939 demethylase 1 (KDM1A/LSD1) impairs colorectal cancer tumorigenesis by affecting cancer cells
940 stemness, motility, and differentiation. Cell Death Discov. 2023; 9: 201.
941 48 Li G, Jiang Y, Tong H, Liu J, Jiang Z, Zhao Y, et al. Sciatic nerve stimulation enhances NK cell
942 cytotoxicity through dopamine signaling and synergizes immunotherapy in triple-negative breast
943 cancer. Drug Resistance Updates. 2025; 79: 101212.
944 49 Chai Q-Q, Li D, Zhang M, Gu Y-W, Li A-X, Wu X, et al. Engineering nanoplatforms of bacterial
945 outer membrane vesicles to overcome cancer therapy resistance. Drug Resistance Updates. 2025; 83:
946 101277.
947 50 Sobczak M, Strachowska M, Gronkowska K, Karwaciak I, Pulaski L, Robaszkiewicz A. LSD1
948 Facilitates Pro-Inflammatory Polarization of Macrophages by Repressing Catalase. Cells. 2021; 10.
949 51 Trehan R, Huang P, Zhu X B, Wang X, Soliman M, Strepay D, et al. SPP1 + macrophages cause
950 exhaustion of tumor-specific T cells in liver metastases. Nat Commun. 2025; 16: 4242.
951 52 Wu Y, Jiang X, Yu Z, Xing Z, Ma Y, Qing H. Mechanisms of Anti-PD Therapy Resistance in
952 Digestive System Neoplasms. Recent Patents on Anti-Cancer Drug Discovery. 2025; 20: 1-25.
953 53 Zheng B, Zhang W, Xie S, Han Y, Liu G, Liu Y, et al. Selinexor as a Therapeutic Target: Advances
954 in Non-small Cell and Small Cell Lung Cancer Treatment Strategies. Recent Patents on Anti-Cancer
955 Drug Discovery. 2025; 20: 274-284.
956 54 Martin M. Cutadapt removes adapter sequences from high-throughput sequencing reads.
957 EMBnet.journal. 2011; 17: 10-12.
958 55 Thrash A, Arick M, Peterson D G. Quack: A quality assurance tool for high throughput sequence
959 data. Analytical Biochemistry. 2018; 548: 38-43.

960 56 Oksanen J, Kindt R, Legendre P, Hara B, Henry M, Stevens H. The Vegan Package. 2007.

961

Supplementary Files

This is a list of supplementary files associated with this preprint. Click to download.

- SupplementaryMaterial.docx